

Novel Approach for Evaluating Detector Systematics in the MicroBooNE LArTPC

MICROBOONE-NOTE-1075-PUB

The MicroBooNE Collaboration*

June 2020

Abstract

One of the primary challenges in current and future precision neutrino experiments using liquid argon time projection chambers (LArTPCs) is understanding detector effects and quantifying the associated systematic uncertainties. MicroBooNE has pioneered the evaluation of detector-related systematic uncertainties for such experiments. This note presents a novel technique for assessing detector systematics based on low-level comparisons between data and simulation. The method can be used to better understand detector-related uncertainties while remaining agnostic to the details of the detector model in simulation. We believe similar approaches could be applied to future LArTPC experiments, including SBN and DUNE.

1 Introduction

Detector systematics quantify the uncertainties on our measurements due to differences between the detector response in simulation and in reality. This note describes a method in which the response of the MicroBooNE LArTPC detector is characterized in data and simulation, and the results are used to modify simulated signals and thus to produce samples of altered simulated events. Comparisons between altered simulations and the nominal simulation can be used to estimate detector systematic uncertainties for physics analyses. This method is used to address uncertainties related to ionization charge in the TPC that can be described by changes in the amplitude and width of signals on the wire waveforms.

For the subset of the detector variations where this approach can be used, it has several advantages over other options. First, it relies only on the output of the simulation and not on the specific models for different components of the microphysics and detector response. It therefore allows us to capture residual effects that are not well-described by existing models or that are not fully simulated. Second, it is relatively computationally efficient. By working with the wire waveforms that are the output of the signal processing stage, this method provides a procedure for generating samples of altered simulated events that is about an order of magnitude faster than running the full simulation.

Section 2 lays out the relevant detector variables and the parameters that we use to characterize the detector's response as a function of those variables. Section 3 describes the samples in data

*Email: microboone_info@fnal.gov

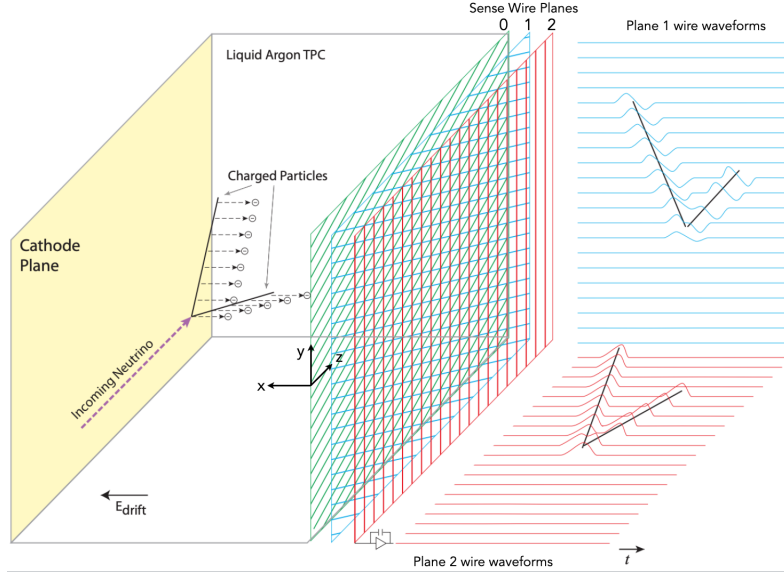


Figure 1: The MicroBooNE detector and operating principles, adapted from [1], as described in the text. The green and blue wire planes are the induction planes; the red wire plane is the collection plane. The right-hand portion of the figure shows the wire waveforms before deconvolution.

and simulation that we will compare in order to characterize the response. Section 4 explains the procedure for extracting the data-to-simulation comparisons, which take the form of ratios of waveform properties, and presents the results. Section 5 describes the application of these ratios to modifying the wire waveforms and producing the altered simulation samples for detector systematics evaluation.

2 Choice of Detector and Waveform Parameters

The MicroBooNE detector [1] is a liquid argon time projection chamber (LArTPC) designed to observe neutrino interactions and is illustrated in Figure 1. When charged particles traverse the detector, they deposit energy that creates ionization electrons and also produces prompt vacuum ultraviolet scintillation photons. The ionization electrons drift in the applied electric field until they reach the three sense wire planes located at the anode. The electrostatic potentials of the wire planes are set up such that ionization electrons pass undisturbed by the first two planes before ultimately ending their trajectory on a wire in the last plane. The drifting electrons induce signals on the first two planes, referred to as induction planes or planes 0 and 1, and then directly contribute to the signals in the final plane, referred to as the collection plane or plane 2. The collection plane wires are aligned vertically and the induction plane wires are oriented at $\pm 60^\circ$ from the vertical. Each wire records its voltage as a function of time to produce a raw waveform. A noise filtering algorithm removes inherent and electronic noise [2], and then the signals are deconvolved [3, 4] to produce a Gaussian waveform that measures the charge that arrived at the wire as a function of time. Scintillation photons are observed by an array of 32 photo-multiplier tubes (PMTs) located behind the wire planes. The optical information is used for triggering the detector.

In general, the detector's response to an energy deposit depends on the position and the amount

of energy deposited, as well as the angular orientation of the particle’s trajectory with respect to the wires [3, 4]. The MicroBooNE coordinate system is defined such that the x axis points along the drift electric field direction from the anode to the cathode, the y axis points vertically up, and the z axis completes a right-handed coordinate system. It is useful to define the detector angles θ_{XZ} and θ_{YZ} for a displacement vector $\Delta\vec{r}$ with components $(\Delta x, \Delta y, \Delta z)$ as below.

$$\begin{aligned}\theta_{XZ} &= \arctan(\Delta x / \Delta z) \\ \theta_{YZ} &= \arctan(\Delta y / \Delta z)\end{aligned}\tag{1}$$

We also denote the amount of ionization energy deposited by a charged particle per unit length by dE/dx . We will characterize the detector’s response as a function of these six variables: x , y , z , θ_{XZ} , θ_{YZ} , and dE/dx . Much of the variability in the detector’s response in y and z is driven by the presence of non-responsive wires in one plane, which can affect the behavior of the signals on the other planes [4], so these two are considered together. The remaining variables are considered independently.

We also need to choose parameters to characterize the detector’s response as a function of the variables above. We can describe the effects of each of the variables on the post-deconvolution wire waveforms in terms of a Gaussian fit to the waveform, called a hit. A hit has an integrated charge Q , measured in $\text{ADC} \cdot \text{ticks}$, and a width σ , measured in time ticks. These quantities are not calibrated. We use these two properties of hits to quantify how the wire waveforms change as a function of the relevant detector variables.

3 Data and Simulation Samples

We seek to determine the hit properties as a function of the variables identified in Section 2 in both data and simulation. We therefore need comparable samples of charged particle tracks in which each of the relevant variables can be reconstructed. Note that in all simulated events, the signals from the simulated particles are overlaid on unbiased cosmic data, which is collected using a random trigger when we have no neutrino beam (with no requirements on the optical information). The cosmic data overlay incorporates the detector noise and cosmic muon backgrounds found in data events. The data for all samples comes from MicroBooNE’s Run 1 period, taken between February and October 2016.

For measurements as a function of the position and angular variables, cosmic ray muon tracks provide an abundant and well-understood sample. These are selected from our beam-off data, which is collected using the same optical trigger as the beam-on data but when there is no neutrino beam. We need a subset of such muons with a reconstructable x position. This is achieved by using cosmic tracks that are topologically consistent with having crossed the anode or the cathode in-time with the flash of scintillation light that triggered the beam-off event. In addition, the opposite end of the track is required to have crossed either the opposite face of the detector or the top or bottom. These are called anode/cathode piercing tracks (ACPT) and are illustrated in Figure 2. Such through-going cosmic muon tracks generally behave as minimum ionizing particles along their entire length and therefore make a good standard candle. We generate a comparable sample of tracks using CORSIKA [5] for the simulated in-time ACPT muon. Note that the geometrical requirements of this selection combined with the fact that cosmic muons are mostly downward-going imply that the trajectories of ACPT muons tend to populate the regions of the detector at low and high x .

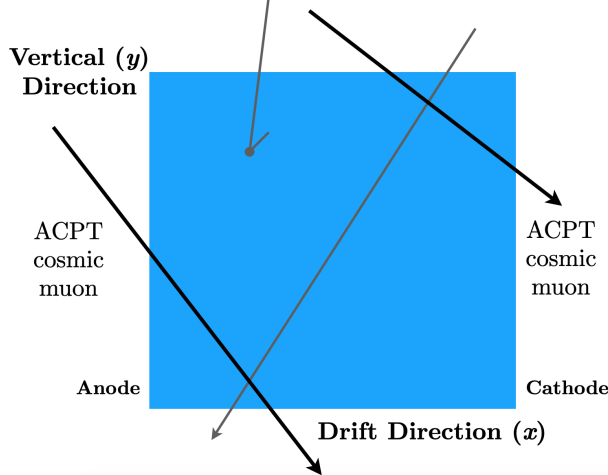


Figure 2: Illustration of two examples of anode/cathode piercing tracks (ACPT), shown in black. The track must cross at least one of the anode or the cathode. The other tracks, shown in gray, are cosmic muons that do not satisfy the ACPT criteria.

For dE/dx , we are interested in the full range of dE/dx values relevant in the MicroBooNE experiment, including highly-ionizing particles such as protons. This motivates us to use a sample of proton tracks identified in neutrino interactions from the Booster Neutrino Beam (BNB). We use proton candidates from ν_μ charged-current inclusive filtered beam-on BNB data and comparable simulated events. The filter makes use of the Pandora pattern-recognition framework [6] to identify likely neutrino candidates using topological and optical information. Remaining cosmic backgrounds are further reduced using PMT-to-TPC matching and fiducial volume cuts; ν_μ charged-current events are selected using track length and particle identification information to identify the final-state muon. Proton track candidates are selected by requiring that the track be at least 15 cm long and that its reconstructed energy loss profile is consistent with what is expected for a proton, using calorimetric information from all three planes. The proton purity of the selected candidate tracks is $> 88\%$.

4 Ratio Extraction

Using the samples described above, we proceed to extract the ratios of the hit charges and widths as a function of the relevant variables described in Section 2: x , (y, z) , θ_{XZ} and θ_{YZ} , and dE/dx . The procedures for each are described in this section and the results are presented.

4.1 Ratio Extraction in x

First, we consider variations in charge in the x position. This captures drift-dependent effects such as diffusion and drift electron lifetime. It will also capture residual effects related to local deviations in the electric field and their impact on electron-ion recombination.

We use the ACPT muon sample described in Section 2. For each hit associated with a reconstructed ACPT muon, we know the charge and width of the hit as well as the reconstructed x position of the corresponding point along the track's trajectory. The reconstructed position is

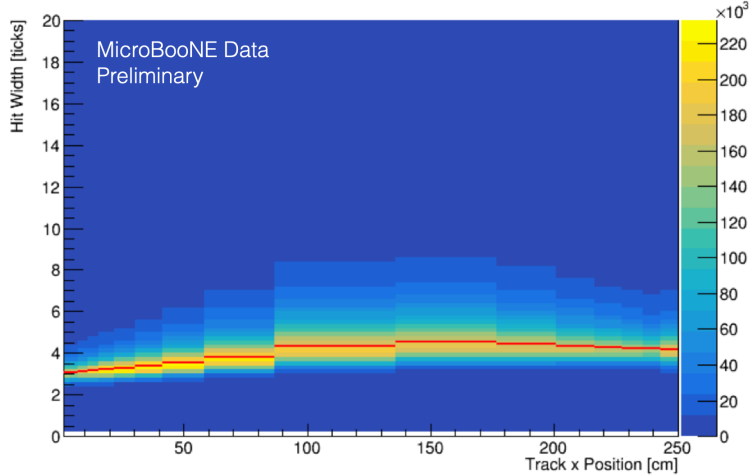


Figure 3: Distribution of hit width vs. x for hits on the collection plane in cosmic data. The color axis indicates the number of hits in a given bin. The red lines indicate the peak in each bin as calculated using the method described in the text.

corrected for local distortions in the electric field using a data-driven field map. This allows us to form 2D distributions of the hit properties vs. x , such as that shown in Figure 3. We make such distributions for hits from each of the three wire planes in both data and simulation.

We then wish to divide the detector up into bins in x . We use a variable binning scheme to ensure a reasonable number of entries in each of the x bins, while allowing for the fact that the ACPT trajectories are concentrated near the anode and the cathode. The binning is the same for the data and simulation, but determined separately for each of the wire planes. Each bin contains hits from several thousand ACPT muons.

Within each bin, the hit properties have some intrinsic spread due to the different properties of their tracks. For example, the distribution of hit widths in one x bin is shown in Figure 4. We seek to average over other sources of variation and measure the variation due to the x position. We do this using an iterative truncated mean algorithm to find the peak of the hit charge and width distributions in each x bin. We start with all the hits in the bin and compute the mean, the median, and the standard deviation. We then remove all hits that are less than 2 standard deviations below the median or more than 1.75 standard deviations above it, and re-calculate all quantities. The boundaries for the truncation reflect the asymmetry of the underlying distributions. We repeat until the calculated mean converges. This calculation is performed in each x bin on each plane in both the cosmic data and the simulation sample. The resulting profiles for hits from the collection plane are shown in Figure 5.

We then take the ratio of the peak in each bin in x in data to that in simulation. To obtain a smooth function that describes these ratios, we perform a spline fit to the measured data points. Figure 6 shows the ratio of the integrated charge and the width of the hits in data compared to simulation as a function of x . The dashed curves are the fitted splines.

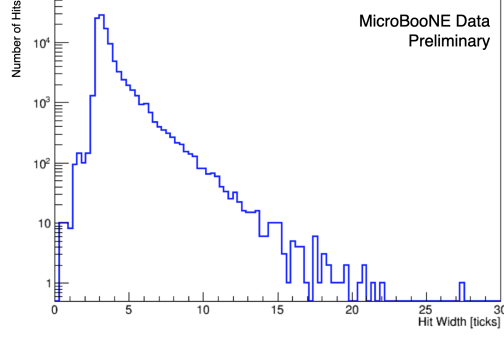


Figure 4: Distribution of hit widths on the collection plane for $1.6 < x < 4.3$ cm in the cosmic data. The spread in the distribution is driven by other sources of variability, such as the position in the yz -plane and the angular orientation of the track. The distribution is asymmetric and is not well-described by a Landau or other simple analytic functions. This motivates us to use the specialized peak-finding algorithm described in the text.

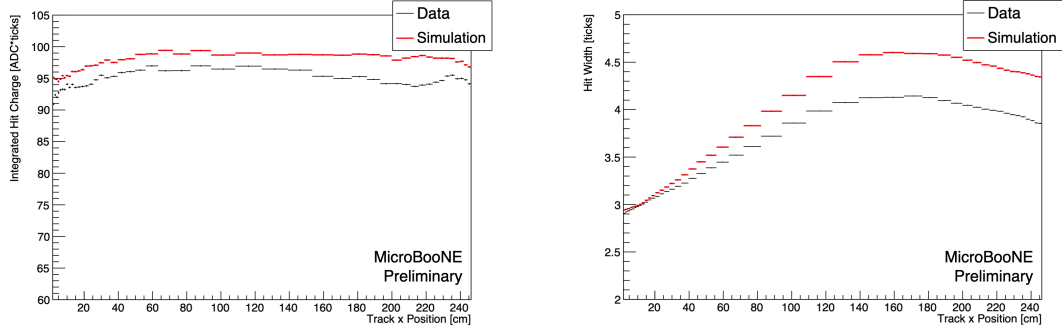


Figure 5: Hit charge and hit width vs. x in data and simulation (MC) for the collection plane. The values are computed from 2D histograms similar to the example shown in Figure 3 using the peak-finding algorithm described in the text.

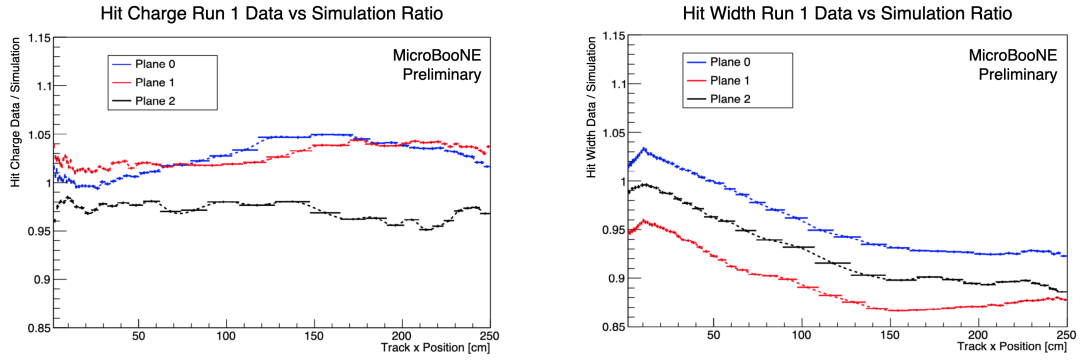


Figure 6: Ratio functions (data/simulation) for hit charge and hit width vs. x on each of the three planes. The solid lines are the bin values, the dashed lines are spline fits. The width of each bin is indicated by the solid horizontal bars.

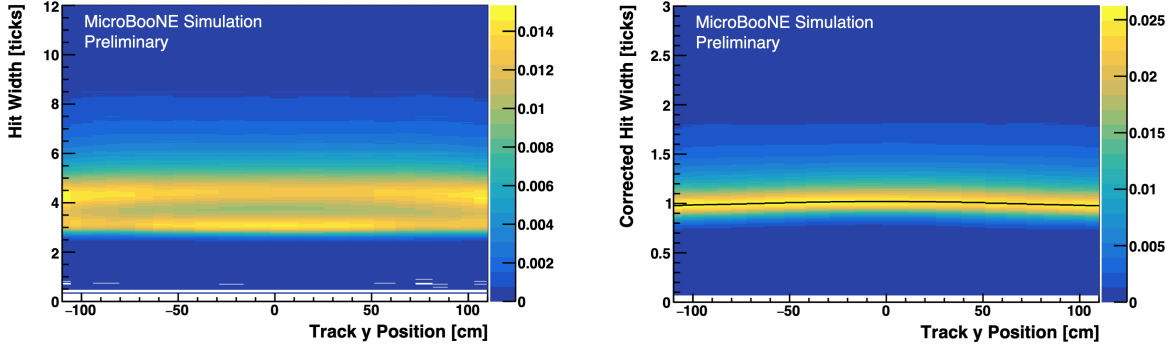


Figure 7: The hit width distribution vs. y position on the first induction plane in the simulation. On the left, this distribution before any correction for the hit width dependence on x . The “double-peak” structure is evident in each of the y bins, where the low-width band comes from ACPT trajectory points near the anode and the high-width band comes from points near the cathode (see Fig. 5). On the right, the x -correction has been applied and the “double-peak” structure is removed. The black curve indicates the peak of the distribution found in each y bin.

4.2 An x Correction for Remaining Ratios

The hit widths show relatively large variations as a function of x , as seen in Figure 5. As a result, the hit widths have a very wide distribution when projected on other variables. Particularly for the ACPT muon sample, in which the trajectories tend to populate the regions of at high and low x , this leads to a “double-peak” structure and makes it very hard to measure the hit width dependence on other variables. An example of this feature is shown in Figure 7.

To account for this, and also to prevent any global normalization offsets from being double-counted in the evaluation of detector systematic uncertainties, the data/simulation ratios for the remaining variables are based on x -corrected hit properties. The correction is done by taking the charge and width of the hit and dividing by the calculated peak of the charge and width distribution at the corresponding x position according to the measurements made in Section 4.1. The functions used for the correction are spline fits to the profile functions like those in Figure 5, for data or simulation and for each plane as appropriate.

The remaining ratios in (y, z) , the angular variables, and dE/dx are all made using these x -corrected hit properties, such that the x ratios contain any global scale offsets. These measurements are further described in the sections below.

4.3 Ratio Extraction in (y, z)

We consider variations in the charge in the yz -plane. This captures effects related to the individual wires’ responses, for example due to proximity to non-responsive wires in other planes. As discussed in Section 2, the variables y and z are considered together because the behavior is largely driven by the behavior of wires, which extend in both dimensions. Note that the detector response in simulation is made to match the non-uniformities in the yz -plane that are observed in data, and that these non-uniformities are generally calibrated out of the reconstructed quantities used in downstream analyses [7]. However, the measurements described here make use of hits that are

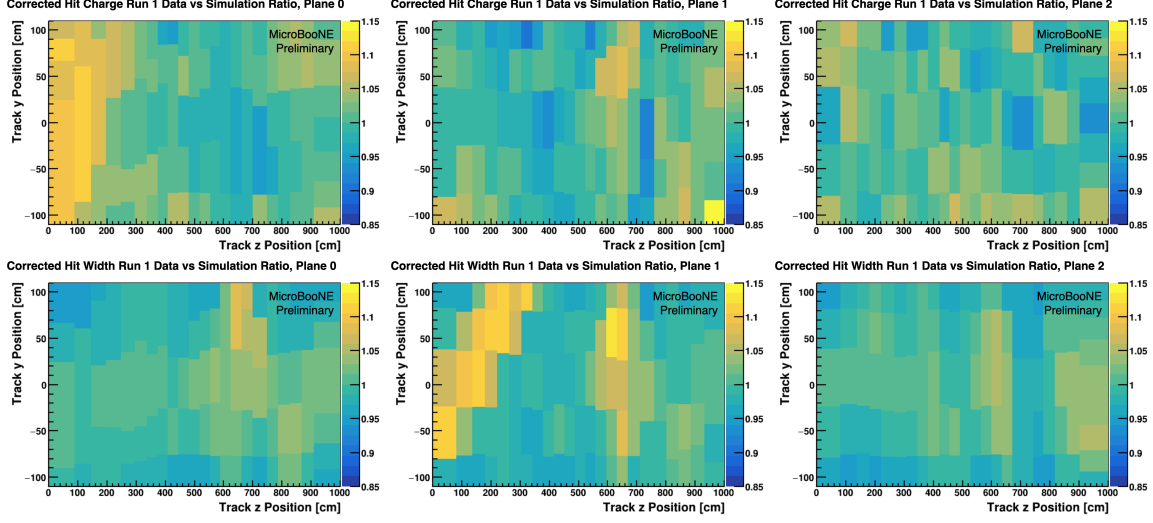


Figure 8: Ratios (data/simulation) for hit charge and width vs. (y, z) . The top plots show the hit charge; the bottom plots show the hit widths. The left-most plots show the ratios on the first induction plane; the middle plots show the ratios on the second induction plane; and the right-most plots show the ratios on the collection plane. Note the color axis is the same on all six plots.

simple Gaussian fits to the deconvolved waveforms and therefore do not include the yz uniformity calibration.

We use the same sample of in-time ACPM muons and the same peak-finding algorithm as described in Section 4.1. However, we now use the x -corrected hit properties as described in Section 4.2. The (y, z) bins are optimized in 2D to again ensure reasonable numbers of entries in each. The result is a set of (y, z) bins that vary in size based on the density of hits on each plane in the different regions of the detector, but they are typically about 4–5 cm² and contain hits from at least a thousand ACPM muons.

With this binning scheme and the x -corrected hit charge and width values, we compute the peak of the hit property distributions in each (y, z) bin in data and simulation. We then take the data/simulation ratio. The results are shown in Figure 8. In order to obtain a smooth function of y and z that describes these ratios, we perform an interpolation between points in the 2D space. In the interior of the detector, the points are the centers of the (y, z) bins. For bins where one edge is along the boundary of the detector, we place an additional point at the midpoint of that edge with the same value as the point at the center of the bin. We also place additional points in the four corners of the (y, z) plane.

4.4 Ratio Extraction in Angular Variables

In addition to the position of the charge in the detector discussed in the preceding sections, we also consider the orientation of the particle trajectory in angular variables. This captures effects related to long-range induced charge signals on the wires as well as the signal processing.

We use the same sample of in-time ACPM muons and the same peak-finding algorithm. We also use the x -corrected hit properties as described in Section 4.2. However, there are special considerations related to the choice of basis for the angular variables and how to handle regions of

angular space where signal processing and hit finding become less reliable.

The two angles relevant for describing the detector response to a charged particle track are the angle with respect to the drift direction and the angle with respect to the wire direction. For the collection plane, where the wires are oriented vertically, these are the angles θ_{XZ} and θ_{YZ} defined in Equation 1, respectively. For the induction planes, where the wires are oriented at $\pm 60^\circ$ from the vertical, we can define the analogous angles with respect to a different set of basis vectors, x' , y' , and z' , where x' remains the drift direction, y' is the appropriate wire direction, and z' completes an orthogonal right-handed basis. Mathematically, we obtain the following expressions for the first (upper sign) and second (lower sign) induction planes.

$$\begin{aligned} x' &= x \\ y' &= 0.5y \pm 0.867z \\ z' &= 0.867y \mp 0.5z \end{aligned} \tag{2}$$

In this document, we refer to the angles as θ_{XZ} and θ_{YZ} for all planes, with the understanding that these quantities always refer to the angle relevant for the plane in question. With this choice of angular basis, the variations in hit properties in θ_{XZ} and θ_{YZ} can be treated independently.

The hit response in both integrated charge and width does not depend on the quadrant for these angles, i.e. that the wire response is independent of the direction (up vs. down, etc.) the particle was traveling as it traversed the detector, as would be expected. Because of this, we are able to “fold” all angles into the space between 0 and $\pi/2$. This is equivalent to taking the absolute value of Δx , Δy , and Δz when computing angles using Equation 1.

With this angular basis, we measure the variations in the x -corrected properties of the hits as a function of the angles. The ACPT muons do not have an isotropic angular distribution, so a variable binning scheme is employed again. We compute the peak in each angular bin in data and simulation using the same algorithm as described in Section 4.1. However, as either θ_{XZ} or θ_{YZ} approach $\pi/2$, the deconvolved waveform corresponding to the extended charge deposition is no longer well-described by a single Gaussian function. Above 1.4 radians (about 80°), we cannot use the observed distribution of hit charges and widths to characterize the detector’s response. We instead extrapolate the ratio between data and simulation between 1.4 radians and $\pi/2$ radians (R_N) using the maximum absolute difference from one over the rest of the angular space (ΔR_{\max}) while maintaining the sign of the difference from the last measured bin (R_{N-1}).

$$\begin{aligned} \Delta R_{\max} &= \max_{\text{bins } k} |R_k - 1| \\ R_N &= 1 + (\text{sign}(R_{N-1} - 1) \cdot \Delta R_{\max}) \end{aligned} \tag{3}$$

Figure 9 shows the ratio of data/simulation for the corrected hit charges and widths as a function of θ_{XZ} , including the extrapolation to the high angle region. For θ_{YZ} , we find that the hit widths have only a weak dependence. We therefore do not extract the ratio of the hit widths as a function of θ_{YZ} and do not apply this as part of our detector systematic uncertainties. Figure 10 shows the ratio of data/simulation for the corrected hit charges as a function of θ_{YZ} .

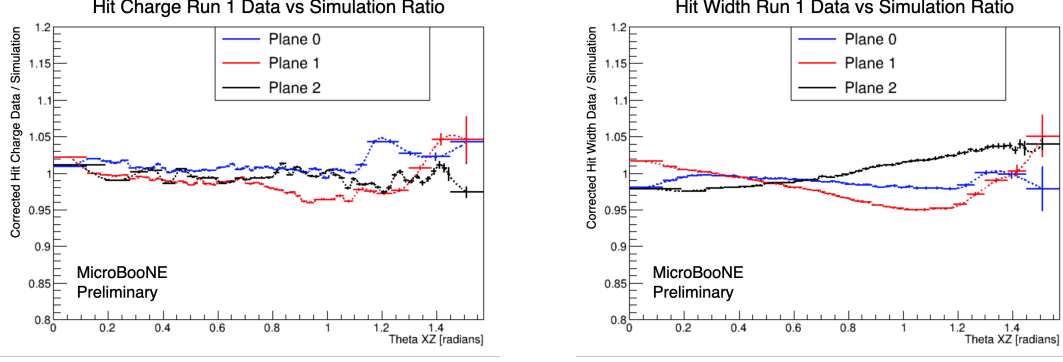


Figure 9: Ratio functions (data/simulation) for hit charge and hit width vs. θ_{XZ} . The solid lines are the values of the ratio in each bin, and the dashed lines are the spline fits. The bins at $1.4 < \theta_{YZ} < \pi/2$ rad are extrapolated as described in the text.

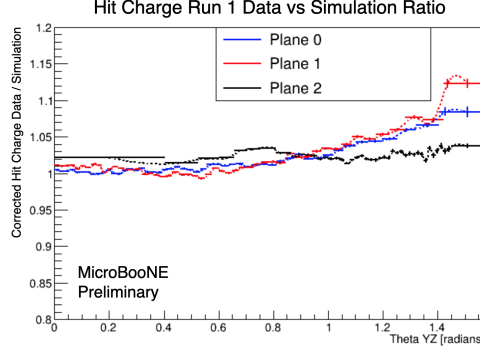


Figure 10: Ratio functions (data/simulation) for hit charge vs. θ_{YZ} . The solid lines are the values of the ratio in each bin, and the dashed lines are the spline fits. The bin at $1.4 < \theta_{YZ} < \pi/2$ rad is extrapolated as described in the text.

4.5 Ratio Extraction in dE/dx

Let us now consider the variation in the waveform due to the amount of local energy deposition, dE/dx , at the corresponding point along the particle's trajectory. This captures effects such as electron-ion recombination, as well as anything else that changes the relationship between dE/dx and the resulting number of observed ionization electrons, dQ/dx .

It is important to make this measurement for the range of dE/dx values important to MicroBooNE analyses. At minimum, we need to cover the range from the minimum ionizing region populated by muons and electrons up to the more highly ionizing region populated by protons. Unlike the previous sections, here we use a sample of proton tracks identified in neutrino interactions, as was described in Section 3. The dE/dx value at each point along the track is calculated using the reconstructed distance from that point to the end of the track, called the residual range, and the Bethe-Bloch formula [8, sec. 33] describing the energy loss of a proton traveling through liquid argon. We perform an empirical fit to the Bethe-Bloch formula and obtain the following

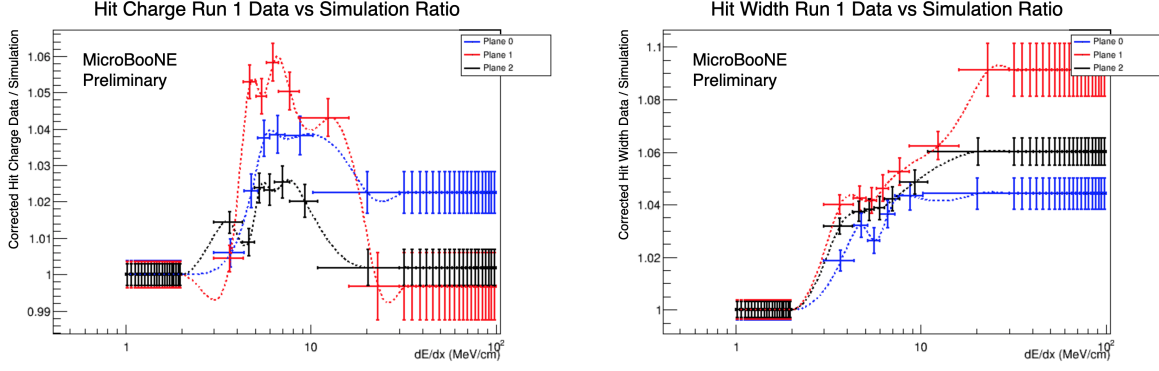


Figure 11: Ratios (data/simulation) for hit charge and width vs. dE/dx . The solid lines are the values of the ratio in each bin, and the dashed lines are the spline fits. The values in the regions below 2 MeV/cm and above 30 MeV/cm are extrapolated described in the text.

relationship, where dE/dx is in units of MeV/cm and the residual range (RR) is in units of cm.

$$\frac{dE}{dx} = -4.32 + \frac{42.2}{\log(2.01 + 4.62 \text{ RR})} \quad (4)$$

In addition to the x correction described in Section 4.2, it is also important to remove bias due to any differences in the angular distribution of the proton tracks between data and simulation. We achieve this by correcting the hit properties in both data and simulation using the measured response as a function of angular variables from Section 4.4. The procedure is analogous to that for the x correction.

Otherwise, we measure variations in the corrected hit properties in much the same way as in the previous sections. The corrected hit charges and widths are binned in the kinematic variable dE/dx (in MeV/cm), calculated from the proton track's residual range as described above. Below 3 MeV/cm, the background contribution is relatively large and the comparison between the data and simulation samples is poor; above 30 MeV/cm, the spatial resolution of the detector is insufficient to measure the residual range. Hits with dE/dx in these two ranges are removed. A variable binning scheme is used to obtain comparable statistics in each of the bins where the measurement is made. Then, analogous to what is done for the other measurements, we profile over the dE/dx distribution using the peak-finding algorithm described in Section 4.1, take the ratio of data/simulation, and perform a spline fit to obtain a smooth function. The ratio points below 2 MeV are set to unity, and smoothly connected to the first measured ratio point at dE/dx of 3 MeV/cm by the spline fit. This avoids double-counting of errors in the minimum ionizing particle region. The ratio points above 30 MeV/cm are set to the value of the ratio in the final measured bin. The extracted ratios and the spline fit to them are shown in Figure 11.

5 Wire Modification

We wish to use the ratio functions extracted in Section 4 to modify the wire waveforms in simulated events so that the detector response is effectively varied. Because the simulated signals are overlaid on unbiased cosmic data, as described in Section 3, we must first identify the simulation-dominated portions of the waveforms.

Each wire signal region can be described by one or more Gaussian functions with a specific position in time ticks, an integrated charge, and a width in time. Such a Gaussian is generally dominated by the ionization charge from a single particle. For each simulated energy deposit in the event, we compute the projected position of the corresponding signal on each wire plane after accounting for local non-uniformities in the electric field. Simulated energy deposits are associated with the Gaussian regions that best match their projected position.

The scale factors that we apply to the wire waveforms are based on the truth information of the simulated energy deposits matched to that portion of the waveform. The individual simulated energy deposits each have an associated amount of energy as well as a start and an end position. We calculate the x , y , and z position of the energy deposit as the average of the start and end positions. The angular variables θ_{XZ} and θ_{YZ} are defined as in Equation 1. The dE/dx is defined simply based on the energy deposited divided by the distance between the start and end positions. Combining these pieces of truth information with the ratio functions derived in Section 4, we can obtain the scale factor for an energy deposit. The charge and width scale values for each Gaussian region of the wires are then computed as the energy-weighted average of the scale values over the associated set of energy deposits. For example, the scale value R for hit widths as a function of x is given by

$$R = \frac{\sum_i E_i \cdot R_\sigma(x_i)}{\sum_i E_i} \quad (5)$$

where the sums are over the set of energy deposits matched to the Gaussian region, E_i is the energy of the i^{th} energy deposit, and $R_\sigma(x_i)$ is the spline fit for the hit widths as a function of x from Figure 6 evaluated at the x position of the i^{th} energy deposit. If a region has little or no matched simulated energy, then the scale factors are set to unity instead. This prevents small amounts of simulated charge from modifying cosmic-dominated regions of the waveforms.

Finally, we use the above information to effectively alter the overall waveform to have the desired integrated charge and width. This is accomplished by modifying the waveform at each time tick using the following procedure. We build an approximation of the original waveform by adding together the Gaussians that describe each region with their original parameters (center t_0 , width σ , and integrated charge Q). Similarly, we build an approximation of the desired post-modification waveform by adding together the Gaussians with the same centers but with modified charge Q' and width σ' based on their computed scale factors. At each tick, we scale the amplitude of the waveform by

$$\text{scale}(t) = \frac{\sum_j \text{Gaus}(t; t_j, Q'_j, \sigma'_j)}{\sum_j \text{Gaus}(t; t_j, Q_j, \sigma_j)} \quad \text{where } \text{Gaus}(t; t_0, Q, \sigma) = \frac{Q}{\sqrt{2\pi}\sigma} \exp\left(-\frac{(t - t_0)^2}{2\sigma^2}\right) \quad (6)$$

where the sums run over the Gaussian region(s) within the relevant wire signal range. Figure 12 shows two examples of how this procedure modifies the waveforms. The final result of running this procedure over an event is a new set of wire waveforms, where signals from simulated charge have been modified but signals from the cosmic data overlay are unchanged.

In order to validate this method, we perform a closure test by taking the ratios extracted from the procedure described above and applying them to the nominal simulation. We then re-extract the ratio functions as described in Section 4 using the wire-modified events produced in place of the nominal simulation. If the method works as expected, the result should be that the ratio functions extracted using the wire-modified samples are flat and equal to unity. We find that this is true to within about $\pm 2\%$ as a function of each of the variables described in Section 2.

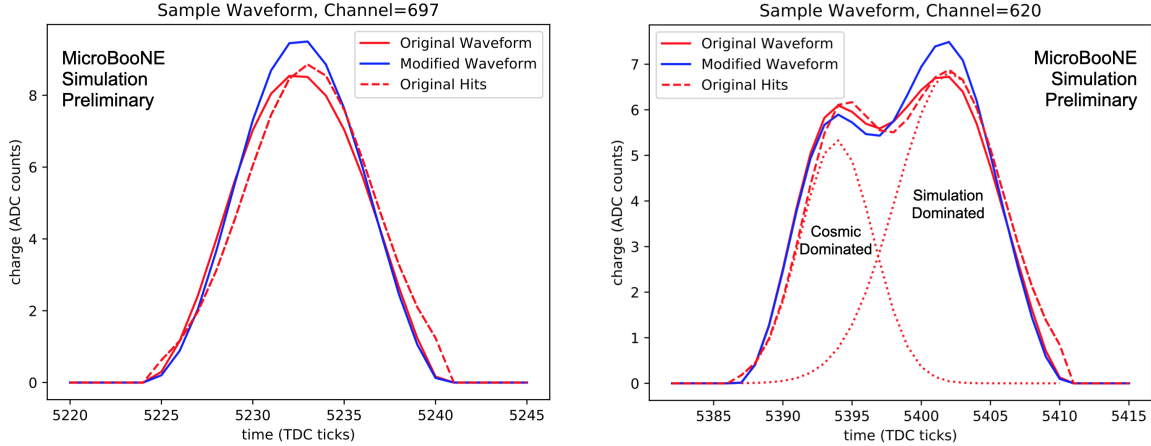


Figure 12: Examples of modified waveforms. The left plot shows a simple example where the wire signal region is well-described by a single Gaussian function. The right plot shows a case where one portion of the waveform is associated to simulated charge while the other is associated with cosmic data charge. Here, the simulation-dominated portion of the waveform is modified but the cosmic-dominated portion is not.

6 Summary and Conclusions

This note has described a novel approach for evaluating a subset of the TPC-related detector systematics in the MicroBooNE LArTPC. This method based on comparisons between the properties of Gaussian hits fitted to the wire waveforms in data and simulation as a function of the relevant variables: x , (y, z) , θ_{XZ} , θ_{YZ} , and dE/dx . The ratios of the waveform properties are used to modify simulated events to produce altered simulation samples, which are then used to quantify detector-related uncertainties. This method is agnostic to the details of the simulation detector model and allows us to capture a number of detector effects that we do understand as well as any “unknown unknowns” that we do not. The detector systematics that are evaluated in this way are complemented by additional variations in the drift electric field and in the scintillation light yield.

Since the publication of MicroBooNE’s first physics results, we have engaged in an extensive campaign to improve our detector modeling [3, 4, 7, 9] and better quantify the associated systematic uncertainties. The work described in this note has been a substantial part of the latter effort. The combination of the improved detector model and the new data-driven approach to systematics evaluation yields reduced uncertainties: from 16.2% in MicroBooNE’s first measurement of the inclusive charged current ν_μ cross section on argon [10], to a preliminary estimate of 3.3% in the most recent measurement of the same [11]. We look forward to bringing out many future results with this improved detector model and its associated systematic uncertainties.

References

- [1] R. Acciarri *et al.* (MicroBooNE Collaboration). “Design and Construction of the MicroBooNE Detector.” *JINST* **12** P02017, 2017. DOI: 10.1088/1748-0221/12/02/P02017.
- [2] R. Acciarri *et al.* (MicroBooNE Collaboration). “Noise Characterization and Filtering in the MicroBooNE Liquid Argon TPC.” *JINST* **12** P08003, 2017. DOI: 10.1088/1748-0221/12/08/P08003.
- [3] C. Adams *et al.* (MicroBooNE Collaboration). “Ionization Electron Signal Processing in Single Phase LArTPCs. Part I. Algorithm Description and Quantitative Evaluation with MicroBooNE Simulation.” *JINST* **13** P07006, 2018. DOI: 10.1088/1748-0221/13/07/P07006.
- [4] C. Adams *et al.* (MicroBooNE Collaboration). “Ionization electron signal processing in single phase LArTPCs. Part II. Data/Simulation Comparison and Performance in MicroBooNE.” *JINST* **13** P07007, 2018. DOI: 10.1088/1748-0221/13/07/P07007.
- [5] D. Heck, J. Knapp, J. N. Capdevielle, G. Schatz, and T. Thouw. “CORSIKA: A Monte Carlo Code to Simulate Extensive Air Showers.” Forschungszentrum Karlsruhe Report FZKA, Report No. FZKA-6019, 1998. URL: ikp.kit.edu/corsika.
- [6] R. Acciarri *et al.* (MicroBooNE Collaboration). “The Pandora Multi-Algorithm Approach to Automated Pattern Recognition of Cosmic-Ray Muon and Neutrino Events in the MicroBooNE Detector.” *Eur. Phys. J. C* **78** 82, 2018. DOI: 10.1140/epjc/s10052-017-5481-6.
- [7] C. Adams *et al.* (MicroBooNE Collaboration). “Calibration of the Charge and Energy Loss per Unit Length of the MicroBooNE Liquid Argon Time Projection Chamber Using Muons and Protons.” *JINST* **15** P03022, 2020. DOI: 10.1088/1748-0221/15/03/P03022.
- [8] M. Tanabashi *et al.* (Particle Data Group). “Review of Particle Physics.” *Phys. Rev. D* **98** 030001, 2018. DOI: 10.1103/PhysRevD.98.030001.
- [9] C. Adams *et al.* (MicroBooNE Collaboration). “A Method to Determine the Electric Field of Liquid Argon Time Projection Chambers Using a UV Laser System and its Application in MicroBooNE.” arXiv:1910.01430 [physics.ins-det]. Link: arxiv.org/abs/1910.01430. Accepted to *JINST*.
- [10] P. Abratenko *et al.* (MicroBooNE Collaboration). “First Measurement of Inclusive Muon Neutrino Charged Current Differential Cross Sections on Argon at $E_\nu \sim 0.8$ GeV with the MicroBooNE Detector.” *Phys. Rev. Lett.* **123** 131801, 2019. DOI: 10.1103/PhysRevLett.123.131801.
- [11] MicroBooNE Collaboration. “Single Differential ν_μ Charged-Current Cross Section with the MicroBooNE Detector Using the Cosmic Ray Tagger.” MICROBOONE-NOTE-1069-PUB. URL: microboone.fnal.gov/wp-content/uploads/MICROBOONE-NOTE-1069-PUB.pdf.